Title
Tuning commensurability in twisted van der Waals bilayers

Permalink
https://escholarship.org/uc/item/9w54m00q

Journal
Nature, 625(7995)

ISSN
0028-0836

Authors
Li, Yanxing
Zhang, Fan
Ha, Viet-Anh
et al.

Publication Date
2024-01-18

DOI
10.1038/s41586-023-06904-w

Peer reviewed

1   **Title: Tuning commensurability in twisted van der Waals bilayers**

2   **Authors:** Yanxing Li[1†], Fan Zhang[1†], Viet-Anh Ha[1, 2], Yu-Chuan Lin[3, 4], Chengye Dong[3], Qiang Gao[1],

3   Zhida Liu[1], Xiaohui Liu[1], Sae Hee Ryu[5], Hyunsue Kim[1], Chris Jozwiak[5], Aaron Bostwick[5], Kenji Watanabe[6],

4   Takashi Taniguchi[6], Bishoy Kousa[1], Xiaoqin Li[1], Eli Rotenberg[5], Eslam Khalaf[1], Joshua A. Robinson[3],

5   Feliciano Giustino[1, 2], Chih-Kang Shih[1*]

6

7   [1]Department of Physics, University of Texas at Austin, Austin, USA

8   [2]Oden Institute for Computational Engineering and Sciences, The University of Texas at Austin, Austin, USA

9   [3]Department of Materials Science and Engineering, Pennsylvania State University, University Park, USA

10   [4]Department of Materials Science and Engineering, National Yang Ming Chiao Tung University, Hsinchu, Taiwan

11   [5]The Molecular Foundry, Lawrence Berkeley National Laboratory, Berkeley, USA

12   [6]Research Center for Materials Nanoarchitectonics, National Institute for Materials Science, Tsukuba, Japan

13   *Corresponding author email: shih@physics.utexas.edu

14

15   **Abstract: Moiré superlattices based on van der Waals materials (vdW) bilayers are created at small**

16   **twist angles leading to a long wavelength pattern with approximate translational symmetry. At large**

17   **twist angles, moiré patterns are, in general, incommensurate apart from a few discrete angles. Here**

18   **we show that large-angle twisted bilayers offer distinctly different new platforms. More specifically**

19   **by using twisted WSe₂ bilayers, we create the incommensurate dodecagon quasicrystals (QC) at $\theta =$**

20   **$30°$ and the commensurate moiré crystals at $\theta = 21.8°$ or $38.2°$. Valley-resolved scanning**

21   **tunneling spectroscopy (STS) unveils disparate behaviors between moiré crystals (with translational**

22   **symmetry) and quasicrystals (with broken translational symmetry). In particular, the K-valley**

23   **exhibits rich electronic structures exemplified by the formation of mini gaps near the valence band**

24   **maximum. These discoveries demonstrate that bilayers with large twist angles offer a new design**

25   **platform to explore moiré physics beyond those formed with small twist angles.**

26   **Main text:**

27   The emergence of moiré superlattice (MSL) designed in van der Waals materials (vdW) bilayers has

28   created unprecedented opportunities to engineer 2D electronic materials with novel properties[1–22]. Thus far,

29   most superlattices investigated are vdW bilayers with small twist angles. At small angles, the moiré

30   wavelength is long, and the pattern is either commensurate or nearly commensurate with the atomic lattices,

31   thus creating a periodically modulated electronic superlattice. At large twist angles, the moiré pattern is in

32   general incommensurate with atomic lattice except for a few angles[23–26]. The incommensurability disrupts

33   the translational symmetry and electronic superlattice is lost. Large angle moiré structures had been largely

34 unexplored until the discovery of dodecagonal quasicrystal in 30° twisted bilayer graphene (tBLG) in

35 2018[27,28]. Although evidence for mini gap formations deep below the Dirac point (DP) has been observed

36 using angle-resolved photoelectron spectroscopy (ARPES), the absence of electronic coupling near the

37 Fermi level, E_F, has limited the effect of quasiperiodicity on other physical properties that are governed

38 primarily by states near E_F in a metallic system. For example, quantum hall effect measurements of 30°

39 tBLG show that the two layers act totally independent[29].

40 Here, we overcome this limitation by using WSe_2 twisted bilayers whose flatter dispersion makes the effects

41 of quasiperiodicity more pronounced at accessible doping[30,31]. We show that large angle twisted WSe_2

42 bilayers offer an interesting platform to explore moiré physics beyond the MSL. We use two modes of STS,

43 constant height and constant current, which allow us to distinguish the momentum space features arising

44 from the K and Γ points. By contrasting the behavior of a large angle commensurate moiré crystal at $\theta_t =$

45 21.8°/38.2° with the 12-fold symmetric 30° incommensurate moiré quasicrystal, we identify several

46 unique properties of the latter. These include the appearance of several Umklapp scattered K-valleys and

47 the existence of a dense set of diffraction spots that preserve the rotational symmetry without the

48 translational symmetry. Remarkably, we are able to resolve signals associated with interlayer Umklapp

49 scatterings up to at least third order suggesting strong interlayer hybridization. For moiré crystals, the new

50 electronic structures are well captured by the first-principle supercell calculations. For moiré quasicrystals,

51 we show that the dense diffraction spots facilitate electron scattering in a manner analogous to a quasi-

52 Bragg plane that couples the Umklapp scattered K-valleys and lead to the formation of a dense set of mini

53 gaps near the valence band maximum. These two moiré structures exemplify the new designer platform

54 enabled at the large twist angles.

55 **Umklapp scatterings in moiré crystal and moiré quasicrystal**

56 Fig. 1a is the experimental schematics with two models shown below, one representing the dodecagonal

57 quasicrystal formed with $\theta_t = 30°$, and the other one the $\sqrt{7} \times \sqrt{7}$ commensurate moiré crystal with $\theta_t =$

58 21.8° (See angle determination in SI Fig. S1). STM images (Fig. 1b and c) indeed reveal the anticipated

59 moiré quasicrystal and the moiré crystal. The corresponding Fast Fourier Transform (FFT) patterns are

60 shown in Fig. 1d and e respectively. Fig. 1d exhibits a dense set of diffraction spots that are rotationally

61 symmetric but without translational symmetry, which is a characteristic of the quasicrystal. By contrast, the

62 diffraction spots of the moiré crystal, are commensurate with the atomic diffraction spots with a scaling

63 ratio of $1/\sqrt{7}$. The dense diffraction spots in Fig. 1d can be analyzed by considering "mutual Umklapp

64 scattering" between the upper and bottom layers, a method previously used for 30° tBLG[27,28] (discussed in

65 SI, Fig. S2&3, Note 1). In our case, up to third-order Umklapp scattering can be identified. As a result, the

66   original K-valleys for individual layers are Umklapp scattered, creating a dense distribution of K-valleys

67   shown in Fig. 2a. As discussed below, the electronic coupling of these K-valleys endows the rich electronic

68   structures associated with the moiré quasicrystals. The distribution of K-valleys in the first quadrant is

69   shown in Fig. 2b where we also label three sets of K-valley pairs (in dashed rectangles). For each pair of

70   K-valleys, an electronic coupling will open a gap which is at the energy degenerate point (anti-crossing),

71   and is schematically shown in Fig. 2c. Fig. 2d is the simulated density of states (DOS) near the gap using

72   the two-band coupling model (See SI Note 2). Below the gap is a paraboloid local maximum while above

73   the gap is a saddle point which leads to a Van Hove singularity (VHS) with logarithmic divergence in DOS.

74   As a consequence of a dense set of diffraction spots in moiré quasicrystals, there are many K-valley pairs

75   whose couplings can lead to anti-crossings and gap openings. One thus expects the formation of many mini

76   gaps in moiré quasicrystals, which correspond to many VHS in DOS.

77   **Observation of VHS from mini gaps in moiré quasicrystal**

78   The electronic structures are investigated using valley-resolved scanning tunneling spectroscopy. Two

79   different modes of STS are simultaneously employed: (a) the conventional constant height STS (CHSTS)

80   and (b) the constant current STS (CCSTS). As discussed previously, K-valley states rapidly decay into the

81   vacuum (due to a large $k_{\parallel}$) and are thus difficult to be detected using CHSTS. This difficulty in detecting

82   the K-valley states can be overcome using the CCSTS.[32] More detailed descriptions of this method can be

83   found in SI Note 3.

84   We first discuss the electronic structures for the moiré quasicrystal in Fig. 3. The STM image for the moiré

85   quasicrystal is shown in Fig. 3a with a few spatial locations marked where tunneling spectra are acquired.

86   The experimental condition to observe quasicrystal structure is discussed in SI Fig. S8. Shown in Fig. 3b

87   are spectra acquired using conventional STS. The two prominent peaks correspond to the two split Γ-valleys

88   resulting from the interlayer coupling. Here we find $\Delta_{\Gamma-\Gamma} = 0.61\ eV$, smaller than the value of $0.75\ eV$

89   observed in the regular R- or H-stacked bilayers (SI Fig. S9, 10). The smaller $\Delta_{\Gamma-\Gamma}$ is due to the reduction

90   of Γ-Γ repulsion at a large twist angle. Due to the rapid decay rate of K-valley states into vacuum, they are

91   very difficult to be detected in the CHSTS mode. In the CCSTS mode, as the sample bias is raised above

92   the highest Γ-state, the tip-to-sample-distance (Z) is automatically adjusted to a smaller value by the

93   feedback to detect the K-valley states (Fig. 3c). As the bias is raised above the VBM, the Z-value is reduced

94   further and the tunneling occurs between the tip and the BLG substrate. Such Z-V plots in the constant

95   current mode delineate different tunneling regimes (Γ-valley, K-valley, and BLG) from which the VBM

96   can also be determined precisely. The fine spectral features in the K-valley are revealed in the differential

97   conductivity $(\partial I/\partial V)_I$ (Fig. 3d-g). One can identify four sharp spectral features (peak 1-4) located at 26,

98   48, 93, and 154 meV below the VBM respectively (Fig. 3d). Among them, peaks 1 and 3 have a clear

99   signature of VHS associated with saddle points above the gap while peaks 2 and 4 are interpreted as the

100   VHS of the paraboloid below the gap (see more evidence in SI Fig. S11). At other spatial locations (Fig.

101   3e-g), spectra show similar structures with some sharp peaks that can be identified as saddle points. As

102   another example in Fig. 3f, the two sharp VHS (saddle points) features occur at 36 meV and 100 meV

103   below the VBM, coincide closely with peaks 1 and 3 in Fig. 3d. The observations of these VHS in tunneling

104   spectra provide unambiguous signatures for the existence of mini gaps due to coupled K-valleys that are

105   Umklapp scattered. If we further interpret peaks 2 and 4 in Fig. 3d as the energy locations below the gap,

106   we can estimate the energy locations (and sizes) of mini gaps at 37 meV (Δ = 21 meV) and 124 meV (Δ =

107   60 meV) below the VBM respectively.

108   We have also carried out nano-ARPES (angle-resolved photoelectron spectroscopy) on exfoliated and

109   stacked WSe_2 bilayers from which we confirm our valley assignments (Extended Data Fig. 1) and observe

110   the band crossing of K_t and K_b occurring at 0.53 eV below the VBM (Extended Data Fig. 2). Given the fact

111   that the energy crossing location is directly proportional to Δk^2 where Δk is the separation of two K-valleys

112   in k-space, we can then estimate the energy locations of mini gaps due to coupling of $K_t^{1m'} - K_b^{1m'}$, $K_t -$

113   $K_t^{1'}$ to be at 36$\pm$5 meV and 134$\pm$20 meV below the VBM (SI Note 4), matching quite well with the

114   experimental observation using STS. The crossing of $K_t^{1'} - K_b^{1'}$ (at 270$\pm$41 meV below VBM) might be

115   too close to the Γ_1 to be visible by STS. More technical details of nano-ARPES investigations are discussed

116   in in SI Note 5.

Interlayer coherent couplings in moiré crystal

118   We next discuss the electronic structure for moiré crystal. The commensurate moiré structures at $\theta_t =$

119   $21.8°$ and $38.2°$ have attracted significant interest in recent years, exemplified by the observation of

120   coherent interlayer transport in BLG[33–35] and coherent interlayer excitons in BL-TMDs[36]. Thus far, however,

121   STM/STS investigations had been lacking. It needs to be noted that for BLG there is no distinction between

122   $\theta_t = 21.8°$ and $38.2°$ because K and K' are degenerate. For BL-TMD, the situation is different because the

123   K/K' degeneracy is lifted.

124   Shown in Fig. 4a is the STM image for a moiré crystal at $\theta_t = 38.2°$. In our investigations, the majority

125   (70%) of commensurate moiré structures are with $\theta_t = 38.2°$ and the minority (30%) with $\theta_t = 21.8°$. In

126   addition, detailed atomic image analysis reveals isotropic strain ranging from +2% to -3% for different

127   moiré crystals (SI Note 6). Conventional STS show similar structures as those observed in moiré

128   quasicrystals where two Γ valleys are observable but not the K-valleys (SI Fig. S22). CCSTS (Fig. 4b), on

129   the other hand, reveals additional structures above the upper Γ-valley. Two clear peaks (peak 1 and 2), with

130   60 meV separation are observed near the VBM. In addition, a weak shoulder (peak 3) is located at ~ 60

131   meV below peak 2. All moiré crystals show very similar spectral features regardless of $\theta_t = 21.8°$ (Fig.

132   4c) or $38.2°$. Moreover, we do not observe sharp VHS associated with saddle points.

133   To aid interpretation of spectral features, we carried out first-principle density functional theory (DFT)

134   calculations. Shown in Fig. 4d are the BZs for the top layer (red), the bottom layer (blue), and the

135   commensurate moiré structure (purple) for a $\theta_t = 21.8°$ ($38.2°$) bilayer. A few critical points (μ, κ and κ')

136   in the moiré BZ (MBZ) are of interest. The two K-valleys, K_t and K_b intersect at the μ point where the anti-

137   crossing is expected. Indeed, the DFT calculation shows a gap of ~ 40 meV opening up at this point, albeit

138   it occurs at an energy level near the Γ_1 state (Fig. 4e). At $21.8°$, all K_t (K_b) valleys are Umklapp scattered

139   to κ (κ') and thus crossing occurs only at the μ point. On the other hand, K'_b and K_t are scattered to the same

140   κ point. At $38.2°$, however, the converse is true. K_t and K'_b will intersect at μ whereas K_t and K_b would be

141   scattered into the same κ point. If spin is conserved after Umklapp scattering, then for $\theta_t = 38.2°$ bilayer,

142   one does not expect anti-crossing occurring at μ, but a K-K splitting at κ. DFT calculations for $\theta_t = 38.2°$

143   bilayer indeed confirm the diminishing gap at μ, but only a small K-K splitting (2 meV) at κ (SI Fig. S25).

144   Experimental investigations in regular bilayers, nevertheless, show significant interlayer K-K coupling[37–

145   40]. Moreover, in MoSe$_2$/WS$_2$ heterobilayers, splitting of moiré exciton states are found near both

146   commensurate angles, indicating that coherent coupling exists for both $K_t- K_b$ and $K_t - K'_b$[10,41]. Another

147   evidence for $K - K'$ coupling is also found in the quasi-particle interference (QPI) analysis (SI note 7).

148   This mechanism provides an explanation of the observation of double peak structure near the VBM for both

149   twisting angles. In addition, it points to a possibility that anti-crossing can also exist for both angles, albeit

150   the energy location is too close to the Γ point to be observed by STS. Then the weak shoulder (peak 3)

151   could be interpreted as the remanent of the VHS (saddle point) above the Γ.

152   In summary, we have studied twisted WSe$_2$ bilayers at large twist angles and discovered distinct behavior

153   of incommensurate 12-fold rotationally symmetric $30°$ moiré quasicrystals and commensurate moiré

154   crystals at 21.8°/38.2° . The former features an aperiodic long-range order which yields a dense set of

155   diffraction spots in k-space. By combining constant height and constant current STM signals, we can

156   resolve the spectral features arising from the K and Γ points. We observe the VHS signatures originating

157   from several mini gaps in the quasi-periodic structure which can be explained using a coupled K-valley

158   model with up to third Umklapp scattering suggesting strong interlayer coupling. For the commensurate

159   21.8°/38.2° structure, two points in the MBZ are of interest: Anti-crossing at the μ point and the coherent

160   coupling at κ-point. The absence of VHS and the double peak structure near the VBM can be interpreted

161   as manifestation of band structures in commensurate moiré crystals. In contrast to previously-studied 30°-

twisted bilayer graphene, the flatter dispersion of our system leads to stronger interlayer coupling at smaller bias voltage making it a very promising platform to study the physics of moiré quasicrystals at finite doping. In addition, the crystallographically-forbidden 12-fold rotation symmetry makes our system distinct from quasi-periodic multilayer moiré systems with multiple unrelated twist angle[42]. Moreover, TMD based moiré quasicrystals is a semiconductor system with strong spin-orbit coupling which endows a rich interplay of valley and spin degrees of freedom that impact both optical and transport properties. The theoretical analysis further shows that such moiré quasicrystals can be generalized to multilayer structures with higher rotation symmetry where the quasiperiodic interlayer coupling can be brought down in energy even further. For example, using tri-layers with two consecutive 20° twists, a new type of quasicrystal with 18-fold rotational symmetry and with an even denser set of diffraction patterns where the mini gaps are expected to occur at smaller doping (SI Fig. S29). This work provides a proof of concept for using large twist angle vdW structures as a new design platform to explore moiré physics beyond those formed at small twist angles.

References:

1. Bistritzer, R. & MacDonald, A. H. Moiré bands in twisted double-layer graphene. *Proc. Natl. Acad. Sci.* **108**, 12233–12237 (2011).

2. Zhang, C. *et al.* Interlayer couplings, Moiré patterns, and 2D electronic superlattices in MoS_2/WSe_2 hetero-bilayers. *Sci. Adv.* **3**, e1601459 (2017).

3. Cao, Y. *et al.* Correlated insulator behaviour at half-filling in magic-angle graphene superlattices. *Nature* **556**, 80–84 (2018).

4. Cao, Y. *et al.* Unconventional superconductivity in magic-angle graphene superlattices. *Nature* **556**, 43–50 (2018).

5. Jin, C. *et al.* Observation of moiré excitons in WSe2/WS2 heterostructure superlattices. *Nature* **567**, 76–80 (2019).

6. Tran, K. *et al.* Evidence for moiré excitons in van der Waals heterostructures. *Nature* **567**, 71–75 (2019).

7. Seyler, K. L. *et al.* Signatures of moiré-trapped valley excitons in MoSe2/WSe2 heterobilayers. *Nature* **567**, 66–70 (2019).

8. Lu, X. *et al.* Superconductors, orbital magnets and correlated states in magic-angle bilayer graphene. *Nature* **574**, 653–657 (2019).

9. Zhang, Z. *et al.* Flat bands in twisted bilayer transition metal dichalcogenides. *Nat. Phys.* **16**, 1093–1096 (2020).

194   10. Zhang, L. *et al.* Twist-angle dependence of moiré excitons in WS2/MoSe2 heterobilayers. *Nat.*
195   *Commun.* **11**, 5888 (2020).

196   11. Wang, L. *et al.* Correlated electronic phases in twisted bilayer transition metal dichalcogenides. *Nat.*
197   *Mater.* **19**, 861–866 (2020).

198   12. Xie, Y. *et al.* Fractional Chern insulators in magic-angle twisted bilayer graphene. *Nature* **600**, 439–
199   443 (2021).

200   13. Li, H. *et al.* Imaging moiré flat bands in three-dimensional reconstructed WSe2/WS2 superlattices.
201   *Nat. Mater.* **20**, 945–950 (2021).

202   14. Bai, Y. *et al.* Excitons in strain-induced one-dimensional moiré potentials at transition metal
203   dichalcogenide heterojunctions. *Nat. Mater.* **19**, 1068–1073 (2020).

204   15. Sharpe, A. L. *et al.* Emergent ferromagnetism near three-quarters filling in twisted bilayer graphene.
205   *Science* **365**, 605–608 (2019).

206   16. Oh, M. *et al.* Evidence for unconventional superconductivity in twisted bilayer graphene. *Nature* **600**,
207   240–245 (2021).

208   17. Li, T. *et al.* Quantum anomalous Hall effect from intertwined moiré bands. *Nature* **600**, 641–646
209   (2021).

210   18. Choi, Y. *et al.* Correlation-driven topological phases in magic-angle twisted bilayer graphene. *Nature*
211   **589**, 536–541 (2021).

212   19. Wang, X. *et al.* Interfacial ferroelectricity in rhombohedral-stacked bilayer transition metal
213   dichalcogenides. *Nat. Nanotechnol.* **17**, 367–371 (2022).

214   20. Törmä, P., Peotta, S. & Bernevig, B. A. Superconductivity, superfluidity and quantum geometry in
215   twisted multilayer systems. *Nat. Rev. Phys.* **4**, 528–542 (2022).

216   21. Weston, A. *et al.* Interfacial ferroelectricity in marginally twisted 2D semiconductors. *Nat.*
217   *Nanotechnol.* **17**, 390–395 (2022).

218   22. Rozhkov, A. V., Sboychakov, A. O., Rakhmanov, A. L. & Nori, F. Electronic properties of graphene-
219   based bilayer systems. *Phys. Rep.* **648**, 1–104 (2016).

220   23. Lopes dos Santos, J. M. B., Peres, N. M. R. & Castro Neto, A. H. Continuum model of the twisted
221   graphene bilayer. *Phys. Rev. B* **86**, 155449 (2012).

222   24. Mele, E. J. Commensuration and interlayer coherence in twisted bilayer graphene. *Phys. Rev. B* **81**,
223   161405 (2010).

224   25. Sboychakov, A. O., Rakhmanov, A. L., Rozhkov, A. V. & Nori, F. Electronic spectrum of twisted bilayer
225   graphene. *Phys. Rev. B* **92**, 075402 (2015).

226   26.   Rozhkov, A. V., Sboychakov, A. O., Rakhmanov, A. L. & Nori, F. Single-electron gap in the spectrum of
227   twisted bilayer graphene. *Phys. Rev. B* **95**, 045119 (2017).

228   27.   Ahn, S. J. *et al.* Dirac electrons in a dodecagonal graphene quasicrystal. *Science* **361**, 782–786 (2018).

229   28.   Yao, W. *et al.* Quasicrystalline 30° twisted bilayer graphene as an incommensurate superlattice with
230   strong interlayer coupling. *Proc. Natl. Acad. Sci.* **115**, 6928–6933 (2018).

231   29.   Pezzini, S. *et al.* 30°-Twisted Bilayer Graphene Quasicrystals from Chemical Vapor Deposition. *Nano*
232   *Lett.* **20**, 3313–3319 (2020).

233   30.   Nguyen, P. V. *et al.* Visualizing electrostatic gating effects in two-dimensional heterostructures.
234   *Nature* **572**, 220–223 (2019).

235   31.   Bisri, S. Z., Shimizu, S., Nakano, M. & Iwasa, Y. Endeavor of Iontronics: From Fundamentals to
236   Applications of Ion-Controlled Electronics. *Adv. Mater.* **29**, 1607054 (2017).

237   32.   Zhang, C. *et al.* Probing Critical Point Energies of Transition Metal Dichalcogenides: Surprising Indirect
238   Gap of Single Layer WSe_2. *Nano Lett.* **15**, 6494–6500 (2015).

239   33.   Koren, E. *et al.* Coherent commensurate electronic states at the interface between misoriented
240   graphene layers. *Nat. Nanotechnol.* **11**, 752–757 (2016).

241   34.   Inbar, A. *et al.* The quantum twisting microscope. *Nature* **614**, 682–687 (2023).

242   35.   Chari, T., Ribeiro-Palau, R., Dean, C. R. & Shepard, K. Resistivity of Rotated Graphite–Graphene
243   Contacts. *Nano Lett.* **16**, 4477–4482 (2016).

244   36.   Zhao, X. *et al.* Strong Moiré Excitons in High-Angle Twisted Transition Metal Dichalcogenide
245   Homobilayers with Robust Commensuration. *Nano Lett.* **22**, 203–210 (2022).

246   37.   Weston, A. *et al.* Atomic reconstruction in twisted bilayers of transition metal dichalcogenides. *Nat.*
247   *Nanotechnol.* **15**, 592–597 (2020).

248   38.   McCreary, K. M. *et al.* Stacking-dependent optical properties in bilayer WSe_2. *Nanoscale* **14**, 147–156
249   (2022).

250   39.   Hsu, W.-T. *et al.* Quantitative determination of interlayer electronic coupling at various critical points
251   in bilayer MoS_2. *Phys. Rev. B* **106**, 125302 (2022).

252   40.   Hsu, W.-T. *et al.* Tailoring excitonic states of van der Waals bilayers through stacking configuration,
253   band alignment, and valley spin. *Sci. Adv.* **5**, eaax7407 (2019).

254   41.   Zhang, Y., Devakul, T. & Fu, L. Spin-textured Chern bands in AB-stacked transition metal
255   dichalcogenide bilayers. *Proc. Natl. Acad. Sci.* **118**, e2112673118 (2021).

256   42.   Uri, A. *et al.* Superconductivity and strong interactions in a tunable moiré quasiperiodic crystal.
257   Preprint at http://arxiv.org/abs/2302.00686 (2023).

258 **Figure captions:**

259 **Figure 1 | WSe$_2$ commensurate moiré crystal and incommensurate moiré quasicrystal. a,** Top: Schematics of the

260 experimental set-up. Bottom: the simulated patterns for 30° incommensurate quasicrystal and 21.8° commensurate

261 moiré crystal. **b,** Typical STM topography for 30° incommensurate quasicrystal (V_{Bias} = 0.3V, I = 30pA). **c,** Typical

262 STM topography for 21.8° commensurate moiré. (V_{Bias} = -0.6V, I = -20pA). **d,** The FFT image of the quasicrystal

263 topography in b with a 6-fold rotational symmetrization. The red circles mark the 12-fold dodecagonal pattern. **e,** The

264 FFT image of the 21.8° commensurate moiré topography in c with a 6-fold rotational symmetrization. The outer and

265 inner dashed hexagons mark the frequency peaks of the WSe$_2$ reciprocal lattice vectors for the Bragg lattice and

266 commensurate moiré crystal, respectively.

267

268 **Figure 2 | Umklapp scatterings and mini gap formation. a,** The schematic of the first 3 orders of Umklapp

269 scatterings near the first BZ for 30° quasicrystal. The red and blue hexagons mark the top and bottom Brillouin zones

270 respectively. The red and blue color dots and circles represent the original K(K') valleys or Umklapp scattered K(K')

271 replicas originated from top and bottom layers respectively. **b,** The distribution of K-valleys in the first quadrant.

272 Three sets of K-valley pair whose couplings can lead to anti-crossing and gap opening are marked in dashed rectangles.

273 **c,** Schematic of a 3D band dispersion showing a mini gap formed by K-valleys' anti-crossing. Where the white and

274 yellow dashed lines represent the gapped band structures in k_x and k_y direction in the momentum space respectively.

275 **d,** Simulated density of states as a function of energy for a typical mini gap. The upper band edge (saddle point)

276 corresponds to a sharp VHS with logarithmic divergence while the lower edge (paraboloid) corresponds to a weak

277 VHS.

278

279 **Figure 3 | Observation of VHS in 30° moiré quasicrystal. a,** STM topography image for a typical 30° quasicrystal

280 region. The black dots mark the sites of the measurement respectively (V_{Bias} = -0.75 V, I = -20 pA). **b,** Large scale and

281 zoom-in (inset) regular constant height dI/dV spectroscopies taken from sites 1 to 4. The light blue arrow and blue

282 arrow mark the Γ_2, Γ_1, respectively (V_{Bias} = -2.0 V / -1.2 V, I = -50 pA / -200 pA). **c,** Zoom-in ZV spectroscopies from

283 sites 1 to 4 (I = -30 pA). **d-g,** Constant current $\partial I/\partial V$ spectroscopies respectively on site 1-4. All peak (shoulder)

284 locations above Γ_1 are marked by red dashed lines. The location of K_{VBM} is indicated with a black dash line (V_{int} = -

285 1.2 V, I = -30 pA, V_{amp} = 10 mV).

286

287 **Figure 4 | Interlayer couplings in 21.8°/38.2° commensurate moiré crystal. a,** STM topography image for a

288 typical 38.2° commensurate moiré crystal region (V_{Bias} = -0.5 V, I = -20 pA). **b,** Gaussian peak fittings for a zoom-in

289 constant current $\partial I/\partial V$ spectroscopies at 38.2° twisted region. The dashed curves represent the fitted peaks (V_{int} = -

290 1.2 V, I = -20 pA, V_{amp} = 15 mV). **c,** Gaussian peak fittings for a zoom-in constant current $\partial I/\partial V$ spectroscopies at

291 21.8° twisted region. The dashed curves represent the fitted peaks (V_{int} = -1.2 V, I = -20 pA, V_{amp} = 15 mV). **d,**

292 Schematic on the left showing the first Brillouin zones (BZs) for 21.8°(38.2°) twisted WSe$_2$ bilayer. The purple, red

293 and black hexagons mark the moiré BZs, top and bottom layer BZs respectively. The K_t, K_t' and K_b, K_b' points of the

294 top (bottom) layer BZ are respectively marked with red and blue circles, $\kappa(\kappa')$ points are marked with purple circles.

295 Schematics on the right show the anti-crossing coupling happened at μ and the coherent coupling at $\kappa(\kappa')$. **e,** DFT

296 calculated unfolded band structure of 21.8° commensurate moiré along the k-space path: $\Gamma - K_t - K_b - K_t' - \kappa' - \kappa$

297 $- \Gamma$. Inset: zoom-in band structure of K_t and K_b band-crossing showing the mini gap.

298

299

300

301

302

303

304

305

306

307

308

309

310

311

312

313

314

315

316

Methods

Sample growth

High-quality buffer on SiC was synthesized via a two-step process. First, monolayer epitaxial graphene was synthesized via silicon sublimation from Si face of semi-insulating SiC substrates (II-VI Inc.). Prior to the growth, SiC substrates were annealed in 10% hydrogen (balance argon) at 1500 ℃ for 30 min to remove subsurface damages due to the chemical and mechanical polishing. Then monolayer epitaxial graphene (MLEG) was formed at 1800 ℃ for 30 min in a pure argon atmosphere. Second, Ni stressor layer was employed to exfoliate the top graphene layer to obtain fresh and high-quality buffer on SiC. 270 nm Ni was e-beam deposited on MLEG with a rate of 5 $\text{Å}/s$ as a stressor layer. Then thermal release tape was used to peel off the top graphene layer from the substrate. The growth of WSe_2 crystals on an EG substrate was carried out at 800 ℃ in a custom-built vertical cold-wall chemical vapor deposition (CVD) reactor for 20 minutes[43]. The tungsten hexacarbonyl ($W(CO)_6$) (99.99%, Sigma-Aldrich) source was kept inside a stainless-steel bubbler where the temperature and pressure of the bubbler were always held at 37 ℃ and 730 Torr, respectively. Mass flow controllers were used to supply H_2 carrier gas to the bubbler to transport $W(CO)_6$ precursor into the CVD chamber. The flow rate of the H_2 gas through the bubbler was maintained at a constant 8 sccm (standard cubic centimeters per minute) which resulted in a $W(CO)_6$ flow rate of 9.0×10^{-4} sccm at the outlet of the bubbler. H_2Se (99.99%, Matheson) gas was supplied from a separate gas manifold and introduced at the inlet of the reactor at a constant flow rate of 30 sccm.

STM/STS measurements

Scanning Tunneling Microscopy and Spectroscopy (STM/S) measurements were conducted at 4.3 K in the STM chamber, with a base pressure$\sim 10^{-11}$ Torr. The W tip was prepared by electrochemical etching and then cleaned by in situ electron-beam heating. STM dI/dV spectra were measured using a standard lock-in technique, whose modulation frequency is 758 Hz. Two different modes of STS were simultaneously employed: (a) the conventional constant height STS (CHSTS) and (b) the constant current STS (CCSTS).

Sample fabrication for nano-ARPES measurements

WSe_2 monolayers, bilayers and hBN layers were exfoliated from high-quality bulk crystals. We use the tear-and-stack method to control the twist angle with an accuracy better than 0.1°. The thickness of bottom hBN layers in all samples is around 3 nm, according to AFM measurements. All samples are firstly annealed at 300 ℃ in an MBE chamber for 30 min with sufficient Se pressure and then annealed at 250 ℃ in an UHV ($\sim 1 \times 10^{-10}\ Torr$) chamber before the ARPES measurement.

nano-ARPES measurements

The experimental setup utilized in this study involved the implementation of nano-ARPES (nano-Angle-Resolved PhotoEmission Spectroscopy) to investigate the electronic structure of the sample. NanoARPES measurements were conducted at the MAESTRO beamline at the Advanced Light source. A capillary mirror obtained from Sigray was employed to achieve a beam size of approximately 1 μm. The measurements were performed at a temperature of approximately 20 K with the R4000 analyzer, equipped with a custom electron deflector, and photon energy of 150 eV was employed during the experiments. To identify the target region, XY scans were conducted with a step size of 0.5 μm. The thickness and the rotation angle of the sample was determined by comparing the intensity of the core level spectrum of O 2s obtained from the natively oxidized silicon substrate, and the valence band structure of the sample.

Theoretical calculation

The Density Functional Theory (DFT) calculations were implemented in the Quantum ESPRESSO suite.[44,45] We employed the PBE exchange-correlation functional[46] in all DFT calculations. The structural optimization was obtained with criteria for force < 0.025 eV/Å, pressure < 0.5 kbar, and total energy $<$ 0.0014 eV. We utilized optimized norm-conserving pseudopotentials[47] from the PseudoDojo library[48] with planewaves kinetic energy cutoff of 98 Ry as recommended. The Van der Waals interaction was taken into account within the semiempirical approach Grimme-D3.[49] The spin-orbit coupling was also included. The unfolded band structures were performed using BandUP code.[50–52]

Method references

43. Lin, Y.-C. *et al.* Realizing Large-Scale, Electronic-Grade Two-Dimensional Semiconductors. *ACS Nano* **12**, 965–975 (2018).

44. Giannozzi, P. *et al.* QUANTUM ESPRESSO: a modular and open-source software project for quantum simulations of materials. *J. Phys. Condens. Matter* **21**, 395502 (2009).

45. Giannozzi, P. *et al.* Advanced capabilities for materials modelling with Quantum ESPRESSO. *J. Phys. Condens. Matter* **29**, 465901 (2017).

46. Perdew, J. P., Burke, K. & Ernzerhof, M. Generalized Gradient Approximation Made Simple. *Phys. Rev. Lett.* **77**, 3865–3868 (1996).

375   47. Hamann, D. R. Optimized norm-conserving Vanderbilt pseudopotentials. *Phys. Rev. B* **88**, 085117

376   (2013).

377   48. van Setten, M. J. *et al.* The PseudoDojo: Training and grading a 85 element optimized norm-conserving

378   pseudopotential table. *Comput. Phys. Commun.* **226**, 39–54 (2018).

379   49. Grimme, S., Antony, J., Ehrlich, S. & Krieg, H. A consistent and accurate *ab initio* parametrization of

380   density functional dispersion correction (DFT-D) for the 94 elements H-Pu. *J. Chem. Phys.* **132**, 154104

381   (2010).

382   50. Medeiros, P. V. C., Stafström, S. & Björk, J. Effects of extrinsic and intrinsic perturbations on the

383   electronic structure of graphene: Retaining an effective primitive cell band structure by band

384   unfolding. *Phys. Rev. B* **89**, 041407 (2014).

385   51. Medeiros, P. V. C., Tsirkin, S. S., Stafström, S. & Björk, J. Unfolding spinor wave functions and

386   expectation values of general operators: Introducing the unfolding-density operator. *Phys. Rev. B* **91**,

387   041116 (2015).

388   52. Iraola, M. *et al.* IrRep: Symmetry eigenvalues and irreducible representations of ab initio band

389   structures. *Comput. Phys. Commun.* **272**, 108226 (2022).

390

391

392

393

394

395

396

397

419 **Author contributions:** C.K.S. conceived the experiment. Y.L. and F.Z. carried out STM/STS
420 measurements. V.H. and F.G. performed DFT calculations. Y.L., C.D., and J.A.R. prepared the MOCVD
421 sample. H.K. helped anneal the sample and perform LEED measurements. Q.G., B.K., and E.K. performed
422 theoretical model calculations. Z. L. and X. Liu. prepared the exfoliated sample. X. Li. involved in the
423 discussion. K.W. and T.T. synthesized the hBN bulk crystals. S. H. R. and E.R. performed the nano ARPES
424 measurement and analyzed the ARPES data. C. J. and A. B. helped with the nano ARPES setup. Y.L., F.Z.,
425 and C.K.S. analyzed the STM data. Y.L., F.Z. and C.K.S. wrote the manuscript with substantial
426 contributions from all the authors. [†]These authors contribute equally to this work.

427 **Competing Interests:** All the authors declare no competing interests.

428 **Data Availability:** Source data that reproduces the plots in the main text and extended data figures are
429 provided with this paper. Source data that reproduce the plots in supplementary information are available
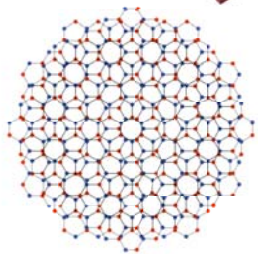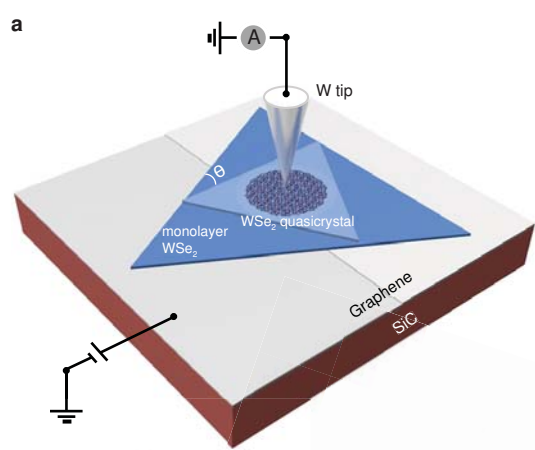430 upon request.

431   **Code Availability:** Source codes used in the manuscript are provided with the paper. The DFT calculations

432   presented in the paper were carried out using publicly available electronic structure codes (referenced in

433   Methods). All other codes in supplementary information are available upon reasonable request.
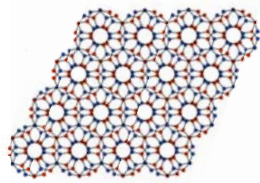
434

435   **Extended Data Figure captions**

436   **Extended Data Figure 1 | Comparison of valley assignments between CCSTS and nano-ARPES. a,**

437   The zoom-in CCSTS taken on quasicrystal. (same as Fig. 3d) **b,** The zoom in K-valley spectrum from the

438   nano-ARPES measurements. **c,** The zoom in Γ-valley spectrum from the nano-ARPES measurements.

439   **Extended Data Figure 2 | nano-ARPES results for quasicrystal. a,** The constant energy surface at E = -

440   1.9 eV. The trigonal K-valleys are labeled by the blue and red solid dots. The blue and red hole circles label

441   the expected locations of the 1st-order Umklapp scatterings. However, no clear features of Umklapp

442   replicas are observed. **b,** Energy distribution curve (EDC) across the center of Γ. Two peaks represent Γ_1 (-

443   1.97 eV) and Γ_2 (-2.44 eV) respectively. **c,** The measured band structure across the center of Γ (k_y=0 Å^{-1}).

444   **d,** The measured band structure across the center of K (k_y=-0.4 Å^{-1}), the K_{VBM} is estimated to be at -1.7 eV.

445   **e,** The measured band structure along the K_t-K_b direction (k_x=-1.4 Å^{-1}) shows the bands crossing. The

446   energy level of the crossing point is determined by the saddle point, at E = -2.23 eV.

a

W tip

θ

monolayer WSe₂

WSe₂ quasicrystal

Graphene

SiC

30° moiré quasicrystal

21.8° moiré crystal

b

2 nm

c

1 nm

d

2 nm⁻¹

e

2 nm⁻¹

a

K_t K_b 1_m
K_t'
K_b'
Γ

b

$K_t^{1m'}$ $K_b^{1m'}$
K_t K_b 1st mirror
$K_t^{1'}$ $K_b^{1'}$ 1st
3rd
K_t'
2nd
Γ K_b'

c

E
Δ
k_y
k_x

d

VHS (Saddle point)
— Above gap
— Below gap
VHS (Paraboloid)
Δ
DOS (a.u.)
E(eV)

a

Site 1
Site 2
Site 3
Site 4

1nm

b

site 1
site 2
site 3
site 4

Γ_2
Γ_1

dI/dV (a.u.)

Bias (V)

c

K-valley

site 1
site 2
site 3
site 4

VBM

BLG

Z (nm)

Bias (V)

d

K-valley

Γ_1

3
1
2
4

$(\partial I/\partial V)_l$ (a.u.)

Bias (V)

e

Γ_1

$(\partial I/\partial V)_l$ (a.u.)

Bias (V)

f

Γ_1

$(\partial I/\partial V)_l$ (a.u.)

Bias (V)

g

Γ_1

$(\partial I/\partial V)_l$ (a.u.)

Bias (V)

a

1 nm

b

38.2° twist

$(\partial I/\partial V)_I$ (a.u.)

Γ₁

Peak 2

Peak 3

Peak 1

Bias (V)

c

21.8° twist

$(\partial I/\partial V)_I$ (a.u.)

Γ₁

Peak 2

Peak 1

Peak 3

Bias (V)

d

$K_b'(K_b)$ K_t μ $K_b(K_b')$

$\kappa\ (\kappa')$

$\Gamma\ (\gamma)$ μ μ'

$\kappa'\ (\kappa)$

K_t'

21.8° (38.2°)

μ

$\kappa\ (\kappa')$

e

$E-E_{VBM}$ (eV)

Γ K_t K_b K_t' κ' κ Γ